

A high-resolution microchip optomechanical accelerometer

Alexander G. Krause^{1†}, Martin Winger^{1†}, Tim D. Blasius^{1†}, Qiang Lin² and Oskar Painter^{1*}

The monitoring of acceleration is essential for a variety of applications ranging from inertial navigation to consumer electronics^{1,2}. Typical accelerometer operation involves the sensitive displacement measurement of a flexibly mounted test mass, which can be realized using capacitive^{3,4}, piezo-electric⁵, tunnel-current^{6,7} or optical^{8–11} methods. Although optical detection provides superior displacement resolution⁸, resilience to electromagnetic interference and long-range readout⁷, current optical accelerometers either do not allow for chip-scale integration or utilize relatively bulky test mass sensors of low bandwidth^{8–10}. Here, we demonstrate an optomechanical accelerometer that makes use of ultrasensitive displacement readout using a photonic-crystal nanocavity¹² monolithically integrated with a nanotethered test mass of high mechanical Q-factor¹³. This device achieves an acceleration resolution of $10 \mu\text{g Hz}^{-1/2}$ with submilliwatt optical power, bandwidth greater than 20 kHz and a dynamic range of greater than 40 dB. Moreover, the nanogram test masses used here allow for strong optomechanical backaction^{14–17}, setting the stage for a new class of motional sensors.

Owing to the rapid development of silicon micromachining technology, microelectromechanical systems (MEMS) accelerometers have become exceedingly popular over the past two decades¹. Evolving from airbag deployment sensors in automobiles to tilt sensors in cameras and consumer electronics products, they can now be found in a large variety of technological applications with very diverse requirements for their performance metrics. For example, sensors for inertial navigation systems require low noise levels and superior bias stability¹⁸, but large bandwidth is crucial for sensors in acoustics and vibrometry applications¹⁹. However, there is a fundamental tradeoff between noise performance and bandwidth that can be understood from the basic principle of operation of an accelerometer (Fig. 1a). When subjected to an acceleration $a(\omega)$ at frequency ω , a mechanically compliant test mass experiences a displacement $x(\omega) = \chi(\omega)a(\omega)$ proportional to the mechanical susceptibility $\chi^{-1}(\omega) = \omega_m^2 - \omega^2 + i[(\omega\omega_m)/Q_m]$. Here, $\omega_m = 2\pi f_m = \sqrt{k/m}$ is the (angular) resonance frequency of the oscillator and Q_m is its mechanical Q-factor (see the plot of $|\chi(\omega)| = |x|/a$ in Fig. 1b for $Q_m = 10$). Usually, accelerometers are operated below their fundamental resonance frequency ω_m , where $\chi(\omega) \approx 1/\omega_m^2$ exhibits an almost flat frequency response. This naturally leads to a tradeoff between resolution and bandwidth, because the large resonance frequency required for high-speed operation results in vanishingly small displacements. As a result, the performance of the displacement sensor constitutes a central figure of merit of an accelerometer.

In a cavity optomechanical system, a mechanically compliant electromagnetic cavity is used to resonantly enhance the readout of mechanical motion²⁰ (canonically, the motion of the end

mirror of a Fabry–Perot cavity). Such systems have enabled motion detection measurements with an imprecision at or below the standard quantum limit (SQL)²¹, corresponding to the position uncertainty in the quantum ground state of the mechanical object. Furthermore, the average optical radiation pressure force can be quite large in micro- and nanoscale optomechanical devices, therefore offering the unique capability of controlling the sensor bandwidth via the optical spring effect^{16,17} and the effective temperature of the sensor by means of passive damping¹⁴ or feedback cold-damping^{15,22}.

In this Letter, we utilize an integrated SiN zipper photonic-crystal optomechanical cavity¹² to provide shot-noise-limited readout of mechanical motion with imprecision near the SQL, enabling high-bandwidth and high-resolution acceleration sensing. The resolution of an accelerometer can be quantified by noise-equivalent acceleration, $\text{NEA} = \sqrt{(a_{\text{th}}^2 + a_{\text{det}}^2 + a_{\text{add}}^2)}$, in units of $\text{g Hz}^{-1/2}$ ($1 \text{ g} = 9.81 \text{ m s}^{-2}$). The first term in the NEA arises from thermal Brownian motion of the test mass (Supplementary Section SVI.a)²³ and is given by

$$a_{\text{th}} = \sqrt{\frac{4k_B T \omega_m}{m Q_m}} \quad (1)$$

The remaining two terms arise from the aforementioned displacement readout noise (a_{det}) and added noise (backaction) onto the test mass due to the act of measurement (a_{add} ; Supplementary Section SVI.b). Fundamental to minimizing the NEA is a reduction in the intrinsic thermal noise a_{th} , which, according to equation (1), requires one to maximize the mass–Q product at a given ω_m . In most commercial accelerometers, the Q-factor is relatively low, which demands large test masses for high resolution. In contrast, in the zipper cavity devices presented here, we use nanotether suspension of a nanogram test mass to yield high intrinsic mechanical Q-factors ($>10^6$), and strong thermo-optomechanical backaction to damp and cool the thermal motion of the test mass.

Figure 1c presents a scanning electron microscope (SEM) image of the device studied here, with the test mass structure and nanotethers highlighted in green. The fundamental in-plane mechanical mode of this structure is depicted in Fig. 1e and is measured to have a frequency of $f_m = 27.5 \text{ kHz}$, in good agreement with finite-element method simulations, from which we also extract a motional mass of $m = 10 \times 10^{-12} \text{ kg}$. The measured mechanical Q-factor is $Q_m = 1.4 \times 10^6$ in vacuum (see Methods), which results in an estimated a_{th} of $1.4 \mu\text{g Hz}^{-1/2}$. The region highlighted in pink corresponds to the zipper optical cavity used for monitoring test mass motion, a zoom-in of which can be seen in Fig. 1d. The cavity consists of two patterned photonic-crystal nanobeams, one attached to the test mass (bottom) and one anchored to the bulk (top). The

¹Kavli Nanoscience Institute and Thomas J. Watson, Sr. Laboratory of Applied Physics, California Institute of Technology, Pasadena, California 91125, USA,

²School of Engineering and Applied Sciences, University of Rochester, Rochester, New York 14627, USA, [†]These authors contributed equally to this work.

*e-mail: opainter@caltech.edu

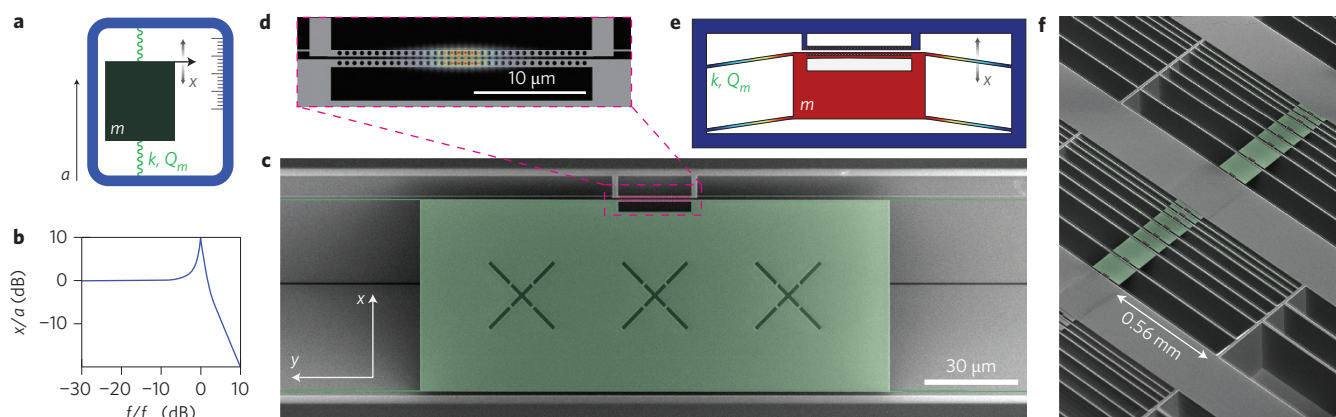


Figure 1 | Overview of accelerometer design. **a**, Canonical example of an accelerometer. When the device (blue frame) experiences a constant acceleration a , a test mass m undergoes a displacement $x = ma/k$. **b**, Frequency response $|\chi(\omega)|$ of an accelerometer on a log-log plot featuring a resonance at $f_m = \sqrt{k/m}/2\pi$ with $Q_m = 10$. **c**, False-coloured SEM image of a typical optomechanical accelerometer. A test mass with dimensions of $150\text{ }\mu\text{m} \times 60\text{ }\mu\text{m} \times 400\text{ nm}$ (green) is suspended on highly stressed 150-nm -wide and $560\text{-}\mu\text{m}$ -long SiN nanotethers, which allow for high oscillator frequencies ($>27\text{ kHz}$) and high mechanical Q -factors ($>10^6$). On the upper edge of the test mass, a zipper photonic-crystal nanocavity (pink) is implemented. The cross-shaped cuts on the test mass facilitate undercutting the device. **d**, Zoom-in of the optical cavity region showing the magnitude of the electric field $|\mathbf{E}(\mathbf{r})|$ for the fundamental bonded mode of the zipper cavity. The top beam is mechanically anchored to the bulk SiN and the bottom beam is attached to the test mass. **e**, Schematic displacement profile (not to scale) of the fundamental in-plane mechanical mode used for acceleration sensing. **f**, SEM image of an array of devices with different test mass sizes.

device in Fig. 1c is designed to operate in the telecom band, with a measured optical resonance at $\lambda_0 = 1,537\text{ nm}$ and an optical Q -factor of $Q_o = 9,500$. With the optical cavity field being largely confined to the slot between the nanobeams, the optical resonance frequency is sensitively coupled to the relative motion of the nanobeams in the plane of the device (the \hat{x} -direction in Fig. 1c). A displacement of the test mass caused by in-plane acceleration of the supporting microchip can then be read out optically using the setup shown in Fig. 2a, where the optical transmission through the photonic-crystal cavity is monitored using an evanescently coupled fibre-taper waveguide²⁴ anchored to the rigid side of the cavity. Using a narrow-bandwidth ($<300\text{ kHz}$) laser source, with laser frequency detuned to the red side of the cavity resonance, fluctuations of the resonance frequency due to motion of the test mass are translated linearly into amplitude fluctuations of the transmitted laser light field (Fig. 2a inset and Supplementary Sections SII and SIII). A balanced detection scheme allows for efficient rejection of laser amplitude noise, yielding shot-noise limited detection for frequencies above $\sim 1\text{ kHz}$.

Figure 2b shows the electronic power spectral density (PSD) of the optically transduced signal obtained from the device in Fig. 1c. The cavity was driven with an incident laser power of $P_{\text{in}} = 116\text{ }\mu\text{W}$, yielding an intracavity photon number of ~ 430 , limited by a thermo-optic bistability. The two peaks around 27.5 kHz arise from thermal Brownian motion of the fundamental in- and out-of-plane mechanical eigenmodes of the suspended test mass. The transduced signal level of the fundamental in-plane resonance, the mode used for acceleration sensing, is consistent with an optomechanical coupling constant of $g_{\text{OM}} = 2\pi \times 5.5\text{ GHz nm}^{-1}$, where $g_{\text{OM}} \equiv \partial\omega_o/\partial x$ is defined as the optical cavity frequency shift per unit displacement. The dotted green line depicts the theoretical thermal noise background of this mode. The series of sharp features between zero frequency (d.c.) and 25 kHz are due to mechanical resonances of the anchored fibre taper (Supplementary Section SVI.f). The noise background level of Fig. 2b is dominated by photon shot noise, an estimate of which is indicated by the red dotted line. The cyan dotted line in Fig. 2b corresponds to the electronic photodetector noise, and the purple dashed line represents the sum of all noise terms. The broad noise at lower frequencies arises from fibre-taper motion and acoustic

pick-up from the environment (Supplementary Section SVI.f). The right-hand axis in Fig. 2b quantifies the optically transduced PSD in units of an equivalent transduced displacement amplitude of the fundamental in-plane mode of the test mass, showing a measured shot-noise-dominated displacement imprecision of $4\text{ fm Hz}^{-1/2}$ (the estimated on-resonance quantum-backaction displacement noise is $23\text{ fm Hz}^{-1/2}$ and the corresponding on-resonance SQL is $2.8\text{ fm Hz}^{-1/2}$; Supplementary Section SVI.b,d).

At this optical power the observed linewidth of the mechanical mode is $\sim 2\text{ Hz}$, approximately 100 times larger than the low-power linewidth. As modelled in the Supplementary Information (Section SV), the measured mechanical damping is a result of radiation pressure dynamical backaction, enhanced by slow thermo-optical tuning of the cavity, which provides the necessary phase lag for efficient velocity damping. Damping of the mechanical resonance is typically used to reduce the ringing transient response of the sensor when subjected to a shock input²⁵. Similar to active feedback damping, this optomechanical backaction also cools the mechanical resonator¹⁵, in contrast to, for instance, gas damping²⁶. The small masses of our device, read out near the SQL, also allow active feedback damping using radiation pressure for device actuation^{15,22}. The measured effective temperature of the fundamental in-plane mode of the test mass, as determined from the area under the 27.5 kHz resonance line in Fig. 2b, is $T_{\text{eff}} \approx 3\text{ K}$. This combination of damping and cooling keeps the ratio of T_{eff}/Q_m fixed, and does not degrade the thermally limited acceleration resolution of the sensor.

To carefully calibrate the accelerometric performance of the device, the sample was mounted on a shake table driven by a shear piezo actuator (see Methods). Applying a sinusoidal voltage to the piezo results in a harmonic acceleration $a(\omega)$, and thus modulation of the transmitted optical power. The optical power in the modulation sideband is given by

$$P_m(\omega) = (1 - T_d) \frac{Q_o}{\omega_o} P_{\text{in}} g_{\text{OM}} |\chi(\omega) a(\omega)| \quad (2)$$

(Supplementary Section SIII), where Q_o is the optical Q -factor (9,500), ω_o is the optical resonance frequency, T_d the relative cavity transmission on resonance (0.88), and the laser is half a linewidth

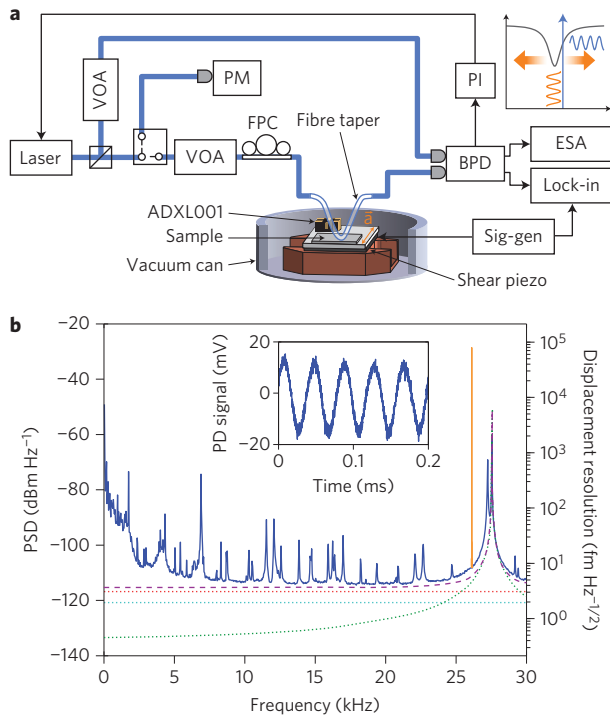


Figure 2 | Experimental system and noise data. **a**, Laser light used to probe the zipper cavity motion is split with a beamsplitter; the signal arm is sent through a fibre polarization controller (FPC) and a fibre taper, which is coupled to the optical cavity, while the other arm is sent directly to a balanced photodetector (BPD). Variable optical attenuators (VOA) in each arm balance the powers, and a power meter (PM) is used to calibrate the probe power. The BPD signal is sent to a proportional-integral controller (PI), locking the laser half a linewidth red-detuned from the optical resonance. The sample is mounted on a shake table comprising a shear piezo. Transduced accelerations are measured using either an electronic spectrum analyser (ESA) or a lock-in amplifier. **b**, Left axis: optical PSD plot of the BPD signal showing mechanical modes at 27.5 kHz. Right axis: equivalent displacement noise. The tone at 26 kHz (orange) is transduction of a tone applied to the shear piezo corresponding to an acceleration of 38.9 mg. The dashed and dotted lines are theoretical noise levels for shot noise (red), detector noise (cyan), thermal noise (green) and the total of all noise contributions (purple). Inset: time trace of the transduction of an applied acceleration of 35.6 mg at 25 kHz.

detuned. The narrow tone at 26 kHz in Fig. 2b (orange) arises from an applied root-mean square (r.m.s.) acceleration of $a_{\text{rms}} = 38.9$ mg, calibrated using two commercial accelerometers mounted on the shake table (see Methods). From the signal-to-noise ratio of this calibration tone we estimate $a_{\text{th}} = 2.0 \mu\text{g Hz}^{-1/2}$, comparable to the theoretical value of $a_{\text{th}} = 1.4 \mu\text{g Hz}^{-1/2}$. For a driving tone at 10 kHz, we measure $a_{\text{min}} \approx 10 \mu\text{g Hz}^{-1/2}$, limited in this case by photon shot noise. The dynamic range over which the sensor is linear at a drive frequency of 10 kHz has also been measured, and is found to be at least 40 dB for this device and >49 dB for a similar device (up to ~ 10 g accelerations, limited by the maximum output voltage of the piezo shaker drive electronics; Supplementary Section SVII).

Figure 3a shows the demodulated photodiode signal normalized to the applied acceleration as a function of drive frequency, corresponding to the frequency-dependent acceleration sensitivity of the zipper cavity (the inset of Fig. 3a presents data from commercial accelerometers used to calibrate the applied acceleration). The dashed red line is the theoretical calculation of the sensitivity without fit parameters and shows excellent agreement. The sharp

Fano-shaped features for lower frequencies can again be attributed to mechanical resonances of the fibre-taper waveguide. The broad region of apparent higher sensitivity around 15 kHz is due to an underestimate of the applied acceleration arising from an acoustic resonance of the shake table.

The calibrated frequency-dependent NEA, shown in Fig. 3b, was obtained by normalizing the ESA noise spectrum (Fig. 2b) with the sensitivity curve (Fig. 3a). Between 25 and 30 kHz, the resolution is limited by the thermal noise of the oscillator, and from 5 to 25 kHz, shot noise limits the resolution to $\sim 10 \mu\text{g Hz}^{-1/2}$. For frequencies lower than 5 kHz, motion of the fibre-taper waveguide and the environment contribute extra noise. The sharp Fano-shaped feature at 27 kHz arises from interference with the fundamental out-of-plane mode of the test mass. The dashed red curve corresponds to a theoretical estimate of the NEA, and shows good agreement. The dashed green line is the fundamental thermal sensing limit.

The device platform demonstrated here straightforwardly allows for further reduction of the NEA. For example, a_{th} can be reduced further by increasing the test mass m . In a preliminary study, we fabricated a series of devices with test masses ranging from 100×10^{-15} kg to 35×10^{-12} kg and recorded their mechanical frequency and Q-factor. Figure 4a depicts the calculated a_{th} versus mechanical frequency of the studied devices, which roughly scales as $a_{\text{th}} \propto \omega_m^{3/2}$ (green line). Adding mass alone also results in a reduction of the sensor bandwidth; however, by scaling the number of nanotether suspensions with test mass size (Fig. 4b,c) the bandwidth can be kept constant. Moreover, as shown in the inset to Fig. 4a, we have found that adding nanotethers does not result in a degradation of the mechanical Q-factor. By simultaneously scaling the width of the test mass and the number of nanotethers, one moves along the orange trend line shown in Fig. 4a (scaling of the device in Fig. 1c by a factor of 100 would yield the grey data point in Fig. 4a at a thermal NEA of $\sim 150 \text{ ng Hz}^{-1/2}$ and a sensor bandwidth of 25 kHz). To show that this scaling is indeed reasonable, we fabricated a device with a test mass of $m = 1.4 \times 10^{-10}$ kg, resulting in a measured Q_m of 1.3×10^6 and corresponding thermal NEA of $410 \text{ ng Hz}^{-1/2}$ (orange data point in Fig. 4a). Using techniques similar to those used in ref. 27, it is straightforward to achieve values of g_{OM} that are ~ 40 times larger than that demonstrated here. Critically, for $g_{\text{OM}} = 2\pi \times 200 \text{ GHz nm}^{-1}$, as measured in previous zipper cavity structures²⁷, the optical input power required to reach this resolution across the entire sensor bandwidth is still submilliwatt.

With a demonstrated acceleration resolution on the order of a few $\mu\text{g Hz}^{-1/2}$ and a bandwidth above 25 kHz, the zipper cavity device presented here shows performance comparable to the best commercial sensors²⁸. These devices, formed from a silicon chip, also allow for the integration of electrostatic tuning capacitors²⁹, thus allowing for the replacement of expensive tunable lasers by cheaper fixed-wavelength sources. Furthermore, fibre-coupled on-chip waveguides¹⁰ and on-chip electronics will enable convenient, small form-factor packaging, as well as facilitating the removal of noise associated with the current fibre taper coupling. In addition, nanoscale optomechanical cavities such as the zipper cavity studied here, offer the unique resource of strong radiation-pressure backaction. The optical spring effect, for example, allows for dynamic tuning of the mechanical resonance frequency, which can increase the low-frequency displacement response (inverse quadratically with frequency) and decrease thermal noise (with the square root of frequency). Similar zipper cavity devices have demonstrated low-power (submilliwatt) optical tuning of the mechanical resonance frequency over tens of megahertz ($>200\%$ of ω_m) into a regime where the mechanical structure is almost entirely suspended by the optical field¹². Also, as shown here, backaction cooling provides a resource to damp the response of the oscillator

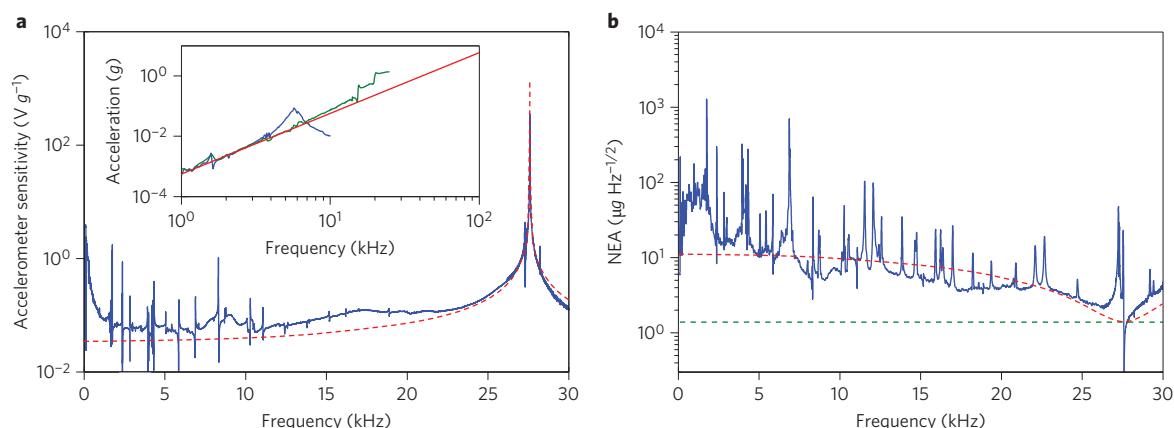


Figure 3 | Frequency-dependence of sensitivity and resolution. **a**, Sensitivity curve as a function of frequency, obtained by driving the shear piezo with a sinusoidal voltage and measuring the amplitude of the resulting voltage modulation of the BPD signal using a lock-in amplifier. The dashed red line corresponds to the theoretical expectation for the sensitivity without fit parameters. Inset: data from commercial accelerometers also attached to the shake table (blue and green curves), which were used for calibrating the applied acceleration (best-fit line, solid red curve). **b**, Frequency-dependent NEA of the device, quantifying its broadband resolution. The plot is obtained by taking the PSD in Fig. 2b and normalizing it with the sensitivity curve in **a**. The dashed red line depicts the theoretical expectation for the NEA given shot noise and thermal noise limitations. The green dashed curve corresponds to the thermal noise (a_{th}).

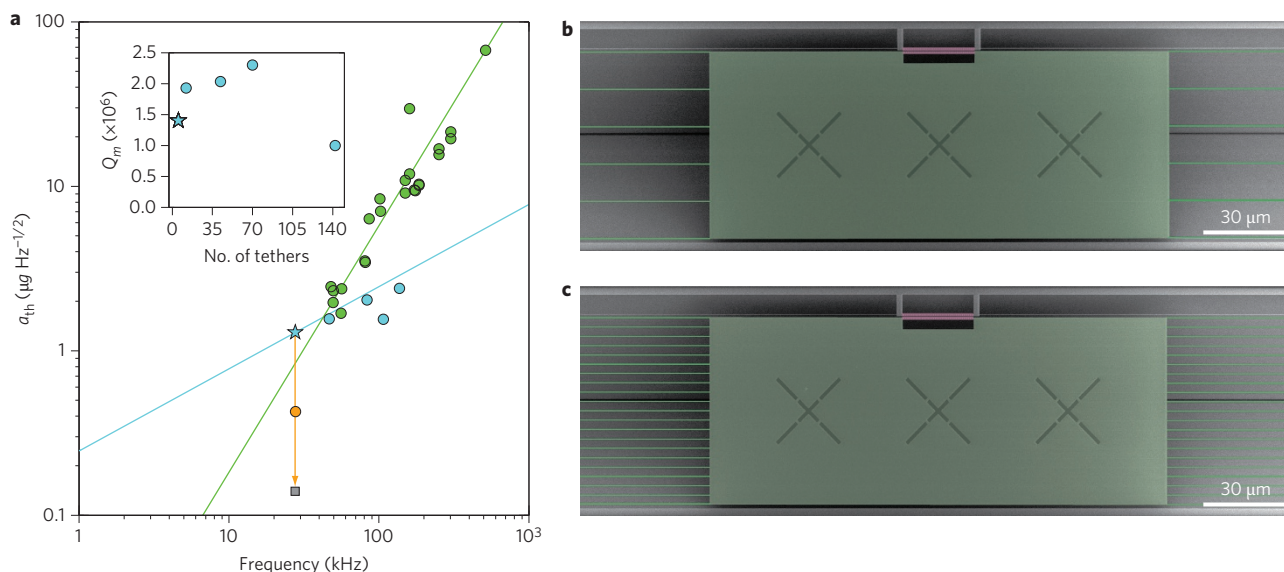


Figure 4 | Independent tuning of bandwidth and resolution. **a**, Thermal acceleration noise density of measured devices (green, cyan and orange data points). The starred point represents the device discussed in the text. The green line is that traversed for adding mass with fixed Q_m and spring constant k , and the cyan line is obtained for varying k while keeping Q_m and m fixed. Varying both m and k allows for independent control of bandwidth and resolution, for example along the orange line, where k/m is constant and Q_m fixed. The grey point represents the theoretical device performance for the test mass increased by a factor of 100 over that in the text. Inset: Q_m for devices corresponding to the cyan circles in **a** versus number of nanotethers attached to the test mass. **b, c**, False-colour SEM images of devices with 12 (**b**) and 42 (**c**) nanotethers and $f_m = 46$ kHz (**b**) and 83 kHz (**c**), respectively.

without compromising the resolution. Combining all of these attributes should allow not only for a new class of chip-scale accelerometers, but other precision displacement-based sensors of, for example, mass, force and rotation.

Methods

Sample fabrication and design. The presented accelerometer structures were defined in a 400-nm-thick SiN layer formed on top of a 500- μ m-thick single-crystal silicon wafer. The SiN was stoichiometric and was grown by low-pressure chemical vapour deposition (LPCVD) under conditions that allowed for large internal tensile stress ($\sigma = 800$ MPa). The accelerometer structures comprising the test mass, the support nanotethers and the zipper cavity were defined in a single electron-beam lithography step. The mask was transferred into the SiN layer using inductively coupled plasma/reactive ion etching (ICP/RIE) dry-etching in SF_6/C_4F_8 plasma. Resist residues were removed in a combination of heated Microposit 1165 remover

and Piranha solution (3:1 $H_2SO_4:H_2O_2$) at 120 °C. The structures were undercut by anisotropic wet-etching in 70 °C hot KOH and cleaned in a second Piranha etching step. Critical point drying in CO_2 avoids collapsing of the zipper cavities.

The optical and mechanical structures were designed using finite-element simulations performed in COMSOL Multiphysics (<http://www.comsol.com/>).

Optical spectroscopy. The sample was optically coupled by means of a near-field probe consisting of a tapered optical fibre. The tapered fibre was brought into optical contact with the device using attocube nanopositioners. Aligned in parallel with the zipper nanobeam, the fibre taper was mechanically anchored on the struts attached to the rigid side of the zipper cavity. Launching light from a NewFocus Velocity tunable external-cavity diode laser into the fibre taper and monitoring the taper transmission then allowed us to carry out resonant coherent spectroscopy of the cavity mode. The technical amplitude noise of the laser (~ 10 dB above the shot noise level) was suppressed by a balanced detection scheme using a Newport 2117 balanced photodetector featuring ~ 20 dB common-mode noise rejection.

Mechanical spectroscopy. Motion of the mechanical oscillator resulted in amplitude-modulation of the laser light transmitted through the fibre taper, which could be measured by monitoring the PSD of the detected balanced-photodiode photocurrent on an electronic spectrum analyser (ESA). Measuring the Q-factors of the mechanical modes is challenging because of the presence of slow frequency drifts of the mechanical mode over frequencies larger than the millihertz mechanical linewidth. To overcome this limitation, we extracted Q_m from the autocorrelation function of the mechanical motion³⁰. To this end, we detected a time trace of the amplitude of thermal oscillations in a bandwidth of ~ 100 Hz using a lock-in amplifier tuned to the mechanical mode frequency. Computing the autocorrelation of these time traces and fitting them to an exponential decay gave us a reliable measure of the mechanical Q-factor. To avoid air-damping, measurements were carried out in vacuum.

Acceleration sensitivity measurement. To apply a.c. accelerations to our device, we constructed a shake table comprising a sample holder plate glued on a shear piezo actuator. Applying a sinusoidal a.c. voltage to the piezo created a displacement $x_0 \sin(\omega_d t)$, resulting in an applied acceleration of $-x_0 \omega_d^2 \sin(\omega_d t)$. For calibration of the shake table assembly, we used commercial accelerometers (Analog Devices) with 5.5 kHz (ADXL103) and 22 kHz (ADXL001) bandwidths. To measure the frequency response of our optomechanical accelerometer, we applied a constant-voltage drive to the piezo and tuned its frequency while measuring the photodetector output on a lock-in amplifier. After normalizing for the ω_d -dependence of the applied acceleration, this yielded the frequency-dependent sensitivity of the device. Normalizing an optical noise PSD then allowed us to calibrate the noise floor of the accelerometer in terms of the NEA.

Received 25 March 2012; accepted 6 September 2012;
published online 14 October 2012

References

1. Krishnan, G., Kshirsagar, C. U., Ananthasuresh, G. K. & Bhat, N. Micromachined high-resolution accelerometers. *J. Indian Inst. Sci.* **87**, 333–361 (2007).
2. Yazdi, N., Ayazi, F. & Najafi, K. Micromachined inertial sensors. *Proc. IEEE* **86**, 1640–1659 (1998).
3. Acar, C. & Shkel, A. M. Experimental evaluation and comparative analysis of commercial variable-capacitance MEMS accelerometers. *J. Micromech. Microeng.* **13**, 634–645 (2003).
4. Kulah, H., Chae, J., Yazdi, N. & Najafi, K. Noise analysis and characterization of a sigma-delta capacitive microaccelerometer. *IEEE J. Solid-State Circ.* **41**, 352–361 (2006).
5. Tadigadapa, S. & Mateti, K. Piezoelectric MEMS sensors: state-of-the-art and perspectives. *Meas. Sci. Technol.* **20**, 092001 (2009).
6. Liu, C. *et al.* Characterization of a high-sensitivity micromachined tunneling accelerometer with micro-g resolution. *J. Microelectromech. Syst.* **7**, 235–244 (1998).
7. Nakstad, H. & Kringelbotn, J. T. Oil and gas applications: probing oil fields. *Nature Photon.* **2**, 147–149 (2008).
8. Krishnamoorthy, U. *et al.* In-plane MEMS-based nano-g accelerometer with sub-wavelength optical resonant sensor. *Sens. Actuat. A* **145–146**, 283–290 (2008).
9. Zandi, K. *et al.* in *2010 IEEE 23rd International Conference on Micro Electro Mechanical Systems (MEMS)* 839–842 (IEEE, 2010).
10. Noell, W. *et al.* Applications of SOI-based optical MEMS. *IEEE J. Sel. Top. Quantum Electron.* **8**, 148–154 (2002).
11. Berkoff, T. A. & Kersey, A. D. Experimental demonstration of a fiber Bragg grating accelerometer. *IEEE Photon. Technol. Lett.* **8**, 1677–1679 (1996).
12. Eichenfield, M., Camacho, R., Chan, J., Vahala, K. J. & Painter, O. A picogram- and nanometre-scale photonic-crystal optomechanical cavity. *Nature* **459**, 550–555 (2009).
13. Verbridge, S. S., Parpia, J. M., Reichenbach, R. B., Bellan, L. M. & Craighead, H. G. High quality factor resonance at room temperature with nanostrings under high tensile stress. *J. Appl. Phys.* **99**, 124304 (2006).
14. Kippenberg, T. J. & Vahala, K. J. Cavity opto-mechanics. *Opt. Express* **15**, 17172–17205 (2007).
15. Genes, C., Vitali, D., Tombesi, P., Gigan, S. & Aspelmeyer, M. Ground-state cooling of a micromechanical oscillator: comparing cold damping and cavity-assisted cooling schemes. *Phys. Rev. A* **77**, 033804 (2008).
16. Corbitt, T. *et al.* Optical dilution and feedback cooling of a gram-scale oscillator to 6.9 mK. *Phys. Rev. Lett.* **99**, 160801 (2007).
17. Lin, Q., Rosenberg, J., Jiang, X., Vahala, K. J. & Painter, O. Mechanical oscillation and cooling actuated by the optical gradient force. *Phys. Rev. Lett.* **103**, 103601 (2009).
18. Zwaehlen, P. *et al.* in *2010 IEEE 23rd International Conference on Micro Electro Mechanical Systems (MEMS)* 631–634 (IEEE, 2010).
19. Endevco (2006) *Accelerometer Selection Based on Applications*, Technical paper 291; available at http://www.endevco.com/news/archivednews/2006/2006_08/2006_08_f4.pdf.
20. Braginsky, V. B. *Measurement of Weak Forces in Physics Experiments* (University of Chicago Press, 1977).
21. Anetsberger, G. *et al.* Measuring nanomechanical motion with an imprecision below the standard quantum limit. *Phys. Rev. A* **82**, 061804(R) (2010).
22. Kleckner, D. & Bouwmeester, D. Sub-kelvin optical cooling of a micromechanical resonator. *Nature* **444**, 75–78 (2006).
23. Yasumura, K. Y. *et al.* Quality factors in micron- and submicron-thick cantilevers. *J. Microelectromech. Syst.* **9**, 117–125 (2000).
24. Michael, C. P., Borselli, M., Johnson, T. J., Chrystal, C. & Painter, O. An optical fiber-taper probe for wafer-scale microphotonic device characterization. *Opt. Express* **15**, 4745–4752 (2007).
25. Li, Y. T., Lee, S. Y. & Pastan, H. L. Air damped capacitance accelerometers and velocimeters. *IEEE Trans. Indust. Electron. Control Instrum.* **IECI-17**, 44–48 (1970).
26. Allen, H. V., Terry, S. C. & De Bruin, D. W. Accelerometer systems with self-testable features. *Sens. Actuat.* **20**, 153–161 (1989).
27. Camacho, R. M., Chan, J., Eichenfield, M. & Painter, O. Characterization of radiation pressure and thermal effects in a nanoscale optomechanical cavity. *Opt. Express* **17**, 15726–15735 (2009).
28. Endevco, Model 752A13 ISOTRON accelerometer; available at <http://www.endevco.com/datasheets/752A1.pdf>.
29. Winger, M. *et al.* A chip-scale integrated cavity-electro-optomechanics platform. *Opt. Express* **19**, 24905–24921 (2011).
30. Stipe, B. C., Mamin, H. J., Stowe, T. D., Kenny, T. W. & Rugar, D. Noncontact friction and force fluctuations between closely spaced bodies. *Phys. Rev. Lett.* **87**, 096801 (2001).

Acknowledgements

This work was supported by the Defense Advanced Research Projects Administration QuASAR program through a grant from the Army Research Office. T.D.B. acknowledges support from the National Science Foundation Graduate Research Fellowship Program (grant no. 0703267).

Author contributions

A.G.K., M.W. and T.D.B. performed sample design, fabrication, optical measurements and data analysis. O.P. and Q.L. developed the device concept and supervised measurements and analysis. All authors worked together on writing the manuscript.

Additional information

Supplementary information is available in the online version of the paper. Reprints and permission information is available online at <http://www.nature.com/reprints>. Correspondence and requests for materials should be addressed to O.P.

Competing financial interests

The authors declare no competing financial interests.